Synthesis by Thermal Decomposition of Two Iron Hydroxyfluorides: Structural Effects of Li Insertion

Kévin Lemoine, Leiting Zhang, Damien Dambournet, Jean-Marc Greneche, Annie Hémon-Ribaud, Marc Leblanc, Olaf Borkiewicz, Jean-marie Tarascon, Vincent Maisonneuve, Jérôme Lhoste

Synthesis by Thermal Decomposition of Two Iron Hydroxyfluorides: Structural Effects of Li insertion

Kévin Lemoine,[†] Leiting Zhang,[‡] Damien Dambournet,[§ #] Jean-Marc Grenèche,[†] Annie Hémon-Ribaud,[†] Marc Leblanc,[†] Olaf J. Borkiewicz,[⊥] Jean-Marie Tarascon,[# ‡] Vincent Maisonneuve,[†] Jérôme Lhoste[* †]

[†] Institut des Molécules et des Matériaux du Mans (IMMM) - UMR CNRS 6283, Le Mans Université, Avenue Olivier Messiaen, 72085 Le Mans Cedex 9, France

[‡] Collège de France, Chaire de Chimie du Solide et de l'Energie, UMR CNRS 8260, 11 Place Marcelin Berthelot, 75231 Paris Cedex 5, France

[§] Sorbonne Universités, Physico-chimie des électrolytes et nano-systèmes interfaciaux, PHENIX, UMR CNRS 8234, 75005 Paris, France

[#] Réseau sur le Stockage Electrochimique de l'Energie (RS2E), FR CNRS 3459, 80039 Amiens, France

[⊥] X-ray Science Division, Advanced Photon Source, Argonne National Laboratory, Argonne, Illinois 60439, United States

ABSTRACT: The synthesis and the electrochemical properties of iron hydroxyfluorides with open-structure, prepared from the thermal decomposition under ambient air of $Fe^{2+}Fe^{3+}F_5(H_2O)_2$ and $Fe^{2+}Fe^{3+}{}_2F_8(H_2O)_2$, are reported. The combination of thermogravimetric analyses, X-ray thermodiffraction (XRD) and Infra-Red spectroscopy has evidenced two instable lacunar oxyfluorides that transform rapidly into hydroxyfluorides under ambient air. Their formulations and structural features have been determined from powder XRD, Mössbauer spectrometry and pair distribution function leading to $Fe^{3+}F_{2.5}(OH)_{0.5}$ with the pyrochlore network and to $Fe^{3+}F_{2.66}(OH)_{0.34}$ with the Hexagonal Tungsten Bronze (HTB) structure. The electrochemistry of these hydroxyfluorides indicates excellent and similar capacities with a significant decrease after the first cycle to reach sustained values of ~110mAh/g upon cycling. *In situ* XRD measurements reveal that the pyrochlore network undergoes amorphisation ($x_{Li+} > 0.5$) while the HTB phase transforms into the ReO_3-type phase ($x_{Li+} > 0.33$).

1. Introduction

Portable electronic devices are becoming prevalent in everyday life and must constantly evolve to cope with increasingly greedy applications. In this scope, the development of high performances electrode materials for lithium-ion batteries (LiBs) is key for achieving more powerful batteries.[1,2] Today's safest option is the lithium-polymer battery with a non-flammable organic electrolyte,[3] coupled with metallic lithium as negative electrode and a metal-transition oxide $LiFePO_4$ having a sustained and reversible capacity of 160 $mA.g^{-1}$. However, having a Li-bearing positive electrode is not mandatory for developing Li metal polymer batteries owing to the presence of Li at the negative electrode. This opens widely the search for alternative high capacity Li-free positive electrodes provided that their composition relies on friendly and abundant chemical elements.[4] Within this context transition metal fluorides associating 3d-block elements to fluorine atoms appear attractive, namely the three-dimensional FeF_3 polymorphs because of their high potential, large theoretical capacities, non-toxicity and low cost attributes.[5,6] Such materials were shown to electrochemically react with Li^+ in two steps. The first one for potentials greater than 2 V vs Li^+/Li is an insertion reaction that enlists the uptake of 1 Li^+ and is associated to the reduction of Fe^{3+}/Fe^{2+}. Then, below 2 V vs Li^+/Li, there is an additional uptake of 2 Li^+ via a conversation reaction process that is associated to the reduction of Fe^{2+} to Fe^0 metal with the concomitant collapse of the structure and formation of LiF. Altogether the electrochemical reduction of FeF_3 leads a total capacity of (712 $mAh.g^{-1}$), hence the interest generated by such phases.[7,8]

Three allotropic varieties of iron (III) trifluoride FeF_3 are known and their structures depend on the packing of FeF_6 octahedral units. The commercially available FeF_3 with ReO_3-type structure

(rhombohedral, *R*-3*c*) which exhibits a dense network containing cavities with narrow windows is the most thermodynamically stable variety.[9] The structures of the other two metastable forms of FeF_3 are built up from hexagonal-tungsten-bronze (HTB) planes with six-membered rings of octahedra to form open framework structures. They contain hexagonal tunnels along the c axis for HTB structure (orthorhombic, *Cmcm*)[10] and interconnected hexagonal channels aligned with [110] and equivalent directions in the pyrochlore structure (cubic, *Fd*-3*m*).[11] These phases rapidly uptake water molecules in their channels with the feasibility to easily release such molecules during a low temperature annealing step.[12] The HTB and pyrochlore structures can be considered with empty cavities. Thus, they become attractive because they exhibit high pore densities with larger windows than the ReO_3 fluoride-type structure, suggesting a more favorable electrochemical reactivity towards Li^+.

The high ionicity of the M-F bond in FeF_3 is beneficial in terms of high voltage but detrimental regarding the electrical properties since this compound is a broad bandgap insulator.[13] To overcome such a conductivity problem inherent to FeF_3 phases, numerous strategies have been explored. The most common one has been to prepare C/FeF_3 composites by ball milling[14] with carbonaceous materials [15,16] being either graphite, CNT, graphene, or OMC.... Similarly, it was found that either Ag or TiO_2 enhances the material properties.[17,18,19] A second approach consists in the preparation of carbon-coated nanosized materials;[20,21] so as to decrease intergranular electrical contacts and therefore decrease the resistivity.[22,23] For example, by doing so a good capacity around 150 $mAh.g^{-1}$ (e.g. removal/uptake of 0.66 Li^+) is obtained for HTB-$FeF_3{\cdot}(H_2O)_{0.33}$ nanoparticles.[24] A third method consists in performing chemical substitution either at the cationic level to reduce the band gap in $M_xFe_{1-x}F_3$ (M = Ti, Co, Cr) for the HTB and pyrochlore varieties[25,26,27] or at the anionic level by partially substituting F^- ions by O^{2-} anions to

reduce the band gap as well. Lastly, the creation of anionic vacancies in iron oxyfluoride with the HTB type structure was successfully prepared by deshydroxylation of iron hydroxyfluoride or by a two step thermal decomposition of $FeF_3{\cdot}3H_2O$ forming $FeF_{3-x}O_{x/2}\square_{x/2}$ where $\square$ refers to anionic vacancy.[28,29] Moreover, Burbano *et al.* have demonstrated that the best electrochemical properties are obtained from a sample containing the higher density of O^{2-} anions and anionic vacancies.[30] Despite a structural modification after the first discharge[31], this material exhibits a good cycling behavior for several cycles with a reversible capacity of 110 $mAh.g^{-1}$.

In light of the aforementioned, we decided to reinvestigate the chemistry of two previously reported compounds $Fe_2F_5(H_2O)_2$ (Fig. 1a) and $Fe_3F_8(H_2O)_2$ (Fig. 1b) that adopt a common structural feature (HTB layer) with the pyrochlore and HTB structures, respectively. They were obtained for the first one by evaporation at 110°C of a solution of a Fe-based aqueous hydrofluoric acid (49%) solution[32] and by hydrothermal synthesis at 400°C and 180 MPa from a mixture of FeF_2 and FeF_3 in aqueous HF (49%)[33-34] for the second one.

Figure 1. View of the structures of $Fe_2F_5(H_2O)_2$ (a) and $Fe_3F_8(H_2O)_2$ (b)

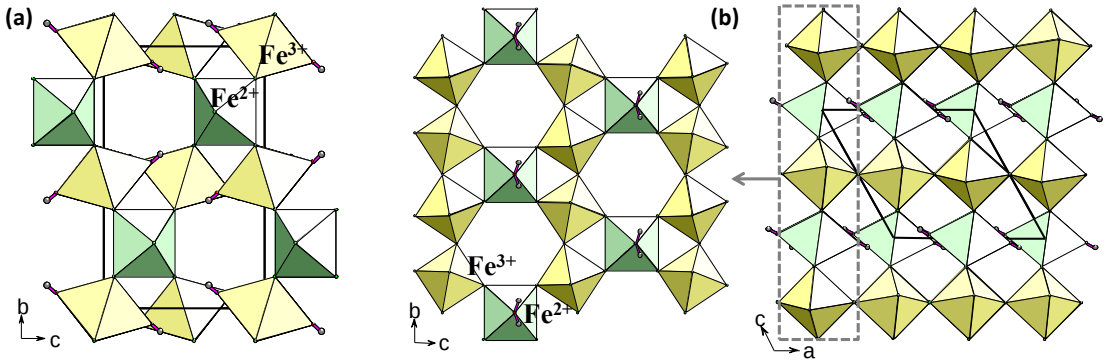

Herein, we report the feasibility to prepare these compounds by a rapid and simple microwave synthesis process. Moreover, these phases are shown to be thermally unstable with the formation, upon special heating treatments, of two new anion-deficient oxyfluorides $Fe^{3+}F_{3-2x}O_x\square_x$ (x = 0.25 and 0.17, respectively) that are unstable under ambient atmosphere and transform

rapidly into stable hydroxyfluorides $Fe^{3+}F_{3-x}(OH)_x$ (x = 0.50 and 0.34, respectively) with pyrochlore and HTB open structures as determined by combined X-ray diffraction Mossbauer and PDF analysis. Lastly, we show that these hydroxyfluorides are electrochemically active with respect to Li with reversible capacities ranging from 100 to 110 $mAh.g^{-1}$.

2. Methodology

2.1 Experimental Methods

The mixed-valence iron fluorides are obtained by solvothermal reaction using a MARS-5 microwave Digestion System (CEM Corp.) from the starting reactants $FeCl_2.4H_2O$ (98%, Alfa Aesar), absolute methanol "MeOH" (99.8%, Sigma Aldrich), deionized water and hydrofluoric acid solution "HF" (27.6 $mol.L^{-1}$, 48%, Riedel De Haen). The safe use of highly hazardous concentrated HF solutions requires wearing gloves (neoprene) and handling inside a fume hood. $Fe_2F_5(H_2O)_2$ is prepared from a mixture of 406 mg $FeCl_2.4H_2O$ (2 mmol), 8.45 mL MeOH, 1 mL H_2O and 0.55 mL HF (15 mmol) corresponding to a molar ratio F/Fe equal to 7.5 and $[Fe^{2+}]$ = 0.2 $mol.L^{-1}$. $Fe_3F_8(H_2O)_2$ is prepared from a mixture of 203 mg $FeCl_2.4H_2O$ (1 mmol), 8.45 mL MeOH, 1 mL H_2O and 0.55 mL HF (15 mmol), corresponding to a molar ratio F/Fe equal to 15 and to $[Fe^{2+}]$ = 0.1 $mol.L^{-1}$. The mixtures are placed in Teflon autoclaves (50 mL) and heated at 160°C for 30 min with stirring. After cooling, the solid products are filtered, washed with technical ethanol and dried at 100°C. They consist of dark brown single crystals of $Fe_2F_5(H_2O)_2$ and a dark microcrystalline powder of $Fe_3F_8(H_2O)_2$.

$Fe_2F_5(H_2O)_2$ and $Fe_3F_8(H_2O)_2$ are then inserted in a furnace under ambient air and heated at 200°C and 300°C, respectively, during 1 h (heating/cooling rate of 2°C/min). They give, after

cooling to room temperature, the brown hydroxyfluorides, $FeF_{2.5}(OH)_{0.5}$ and $FeF_{2.66}(OH)_{0.34}$, respectively.

2.2 Characterizations Methods

2.2.1 Structural and chemical compositions

X-ray diffraction patterns were collected in the range $8° \leq 2\theta \leq 150°$ on a Panalytical MPD-PRO diffractometer equipped with a linear X'celerator detector and a CoK_α radiation (1.789 Å) to avoid the X-ray fluorescence. Rietveld refinements were performed by using the Fullprof profile refinement program.[35,36]

Mössbauer measurements were performed in transmission geometry with a 925 MBq γ-source of $^{57}Co/Rh$ mounted on a conventional constant acceleration drive. The samples with 5 mg Fe/cm^2 were prepared from a softly milled powder. The data were fitted using the MOSFIT program[37] involving quadrupolar and/or magnetic components with lorentzian lines; the isomer shift values are referred to that of α-Fe at RT. The velocity of the source was calibrated using α-Fe as the standard at RT.

High energy X-ray data were collected at the 11-ID-B station at the Advanced Photon Source (Argonne National Laboratory). After corrections (background and Compton scattering), pair distribution functions (PDF) were extracted from the data using PDFgetX2 software.[38] Refinements of the PDF data were performed using PDFgui.[39]

SEM images of the powders and of the sintered pellets were obtained using a JEOL microscope (JSM 6510 LV). Acceleration voltages varied between 20 and 30 kV as a function of the analyzed samples.

2.2.2 Thermal analyses

Thermo Gravimetric Analysis-Mass Spectroscopy (TGA-MS) was performed using a Netzch STA 449 F3 coupled with a QMS 403 C mass spectrometer. The thermoanalytical curves were recorded together with the ion current curves in the multiple ions detection probe. A constant purge gas flow of 80 mL/min nitrogen and a constant heating rate of 5 K/min were applied.

The thermogravimetric (TGA) experiments were carried out with a thermoanalyzer SETARAM TGA 92 with a heating rate of 2 °C.min^{-1} from room temperature up to 900°C under ambient air and dry air (Alphagaz, mixture of oxygen (20%) with nitrogen (80%), H_2O < 3 ppm).

X-ray thermodiffraction (HT-XRD) experiments were performed under dry air flow in an Anton Parr XRK 900 high temperature furnace with the diffractometer already described. The samples were heated from 40 °C to 600 °C at a heating rate of 10 °C min^{-1}. X-ray diffraction patterns were recorded in the 5-60° range with a scan time of 10 min at 10 °C intervals from room temperature to 400 °C and 50 °C intervals from 400 °C to 600 °C.

The powders of $FeF_{2.5}(OH)_{0.5}$ and $FeF_{2.66}(OH)_{0.34}$, were heated in a furnace (Nabertherm LT 3/12/P330) at a heating rate of 3°C.min^{-1} from room temperature to T ≤ 300 °C under ambient atmosphere and were cooled at room temperature. Then, IR spectra were collected (20°C intervals) between 40 cm^{-1} and 4000 cm^{-1} with a scan time of 2 min with an ALPHA FT-IR Spectrometer.

2.2.3 Electrochemistry characterizations

Electrochemical reaction with lithium was evaluated using a Swagelok Li metal cell. FeF_3-based electrodes were composed of 80% active materials and 20% carbon-SP (super pure) as the conductive agent; they were ball-milled using a SPEX Miller 800 at 875 cycles/min for 15 minutes. The area of the electrode was 1 cm^2 with a loading mass of 8 mg. The electrolyte was the commercially LP30 (1M $LiPF_6$). The cell was cycled between 2 and 4 V versus Li^+/Li at C/20 current density.

Notes: After thermal treatment, all phases are immediately outgassed at ambient temperature under secondary vacuum ($P < 10^{-5}$ bar) and stored in a glovebox. It must be noted that all sample preparations for Mössbauer spectrometry, electrochemical characterizations and PDF experiments were realized in a glovebox.

3. Results and discussion

3.1 Synthesis and characterizations of iron hydrated fluorides

Interestingly, the prepared hydrated iron fluorides contain both Fe(II) and Fe(III), while they crystallize from iron(II) chloride and aqueous HF in methanol solvent, hence implying an oxidation process through the reaction. The oxidation of Fe^{2+}, resulting from the presence of water, is governed by two concomitant parameters: the iron concentration and the HF/Fe ratio molar (**Figure 2a**). For low [Fe^{2+}] concentration and high HF/Fe molar ratio, the quantity of water (≈1.25 mL), issued from the aqueous solution of HF and solvents (water/MeOH), promotes the oxidation of Fe^{2+} to Fe^{3+}. Consequently, $Fe_3F_8(H_2O)_2$ (Fe^{3+}/Fe^{2+} = 2) appears preferentially at the expense of $Fe_2F_5(H_2O)_2$ (Fe^{3+}/Fe^{2+} = 1) (**Figure 2b**). Micron-sized cuboid

and polyhedral crystals are observed from scanning electronic microscopy (SEM) for $Fe_2F_5(H_2O)_2$ and $Fe_3F_8(H_2O)_2$ respectively (**Figure 2c**).

Figure 2. Effect of the synthesis parameters on the oxidation of Fe^{2+} to Fe^{3+} (a), XRD patterns of samples obtained using the indicated HF/Fe ratio and [Fe^{2+}] concentrations (b) SEM images of $Fe_2F_5(H_2O)_2$ and $Fe_3F_8(H_2O)_2$ (c)

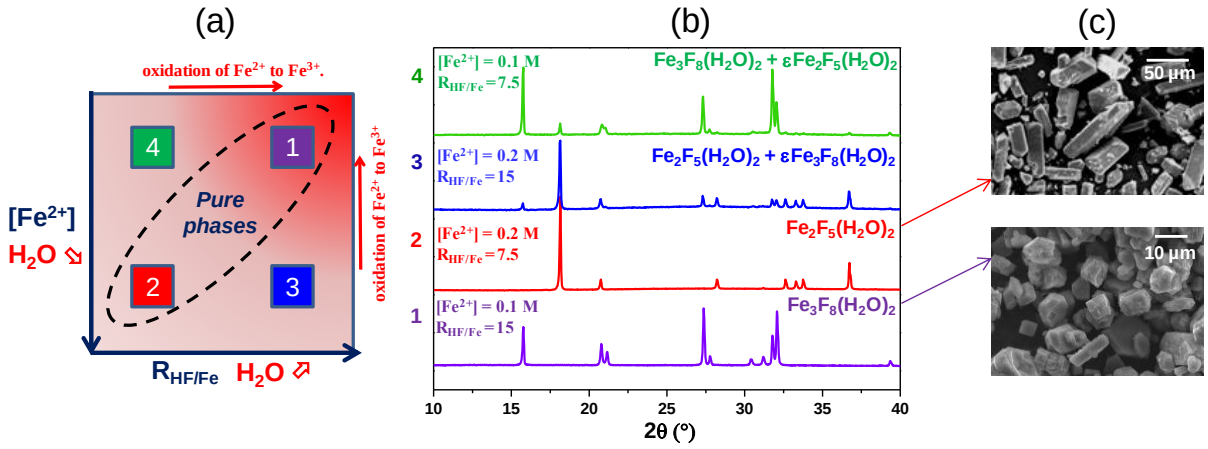

The structure of inverse weberite $Fe_2F_5(H_2O)_2$ was previously determined from single crystals by Laligant *et al* in 1986;[32] the corresponding atomic positions and cell parameters were then introduced in the Rietveld refinement of the powder diffraction data **(Figure 3a)**. Good reliability factors were obtained even if a preferred orientation effect was observed. Refined parameters and atomic positions were close to those estimated by Laligant *et al* **(Table S1, S2)**. The valence states are confirmed from the values of isomer shift estimated from ^{57}Fe Mössbauer experiments. The spectra of $Fe_2F_5(H_2O)_2$ exhibit two paramagnetic contributions **(Figure 3c)** consisting of two well-resolved doublets with lorentzian lines. According to their respective isomer shift values, they are clearly attributed to Fe^{2+} and Fe^{3+} in octahedral coordination **(Table 1)**. In addition, it is concluded that equivalent proportions of Fe^{2+} and Fe^{3+} can be extrapolated

from the isomer shift values obtained at 300 K (47% and 53%) and 77 K (49% and 51%) in conjunction with the temperature evolution of Lamb-Mössbauer factors. The F/Fe ratio ($R_{F/Fe}$ = 2.4) determined from EDX analyses is consistent with the $Fe_2F_5(H_2O)_2$ formulation.

The crystallographic parameters resulting from the Rietveld refinement of $Fe_3F_8(H_2O)_2$ X-ray powder data **(Figure 3b)** are in good agreement with the literature data (**Table S1, S3**).[34] The Mössbauer spectrum at 300 K shows two paramagnetic signatures consisting of well-resolved doublets **(Figure 3d)**. They are attributed to Fe^{2+} and Fe^{3+} in the molar ratio Fe^{3+}/Fe^{2+} = 2. At 77 K, a characteristic Zeeman sextet, resulting of Fe^{3+} magnetic ordering, is observed, while the quadrupole doublet of paramagnetic Fe^{2+} is maintained. These results corroborate the idle spin behavior of $Fe_3F_8(H_2O)_2$ due to magnetic frustration which was demonstrated in [34,]: the Fe^{3+} sublattice is magnetically ordered below T_N = 157 K while Fe^{2+} cations remain paramagnetic down to 35 K.

Figure 3. Final Rietveld profile refinement of X-ray powder diffraction patterns of $Fe_2F_5(H_2O)_2$ (a) and $Fe_3F_8(H_2O)_2$ (b); ^{57}Fe Mössbauer spectra at 300 K and 77 K of $Fe_2F_5(H_2O)_2$ (c) and $Fe_3F_8(H_2O)_2$ (d) (red line for Fe^{2+} and blue line for Fe^{3+}).

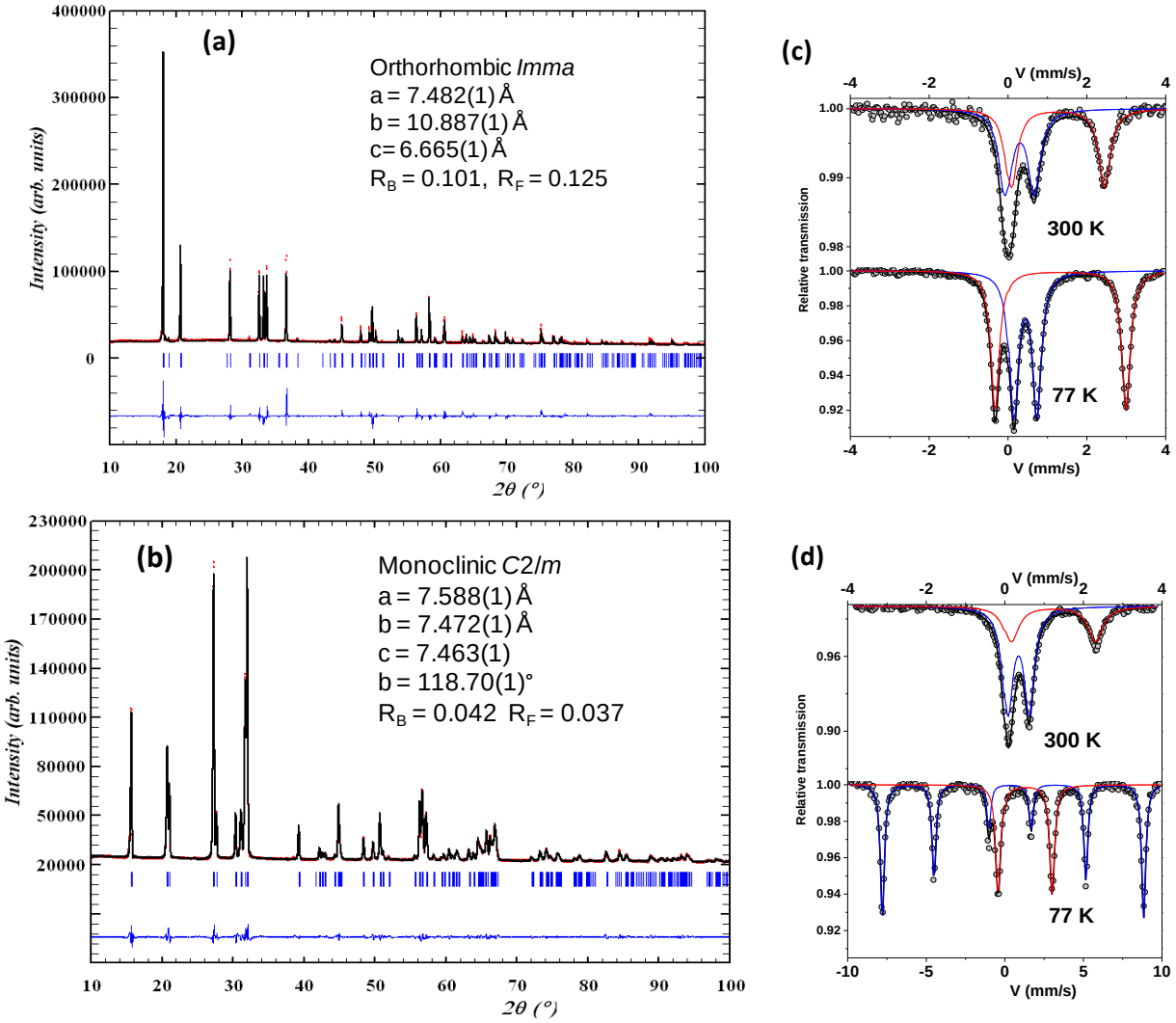

Table 1. Refined values of the hyperfine parameters and line attributions for $Fe_2F_5(H_2O)_2$ and $Fe_3F_8(H_2O)_2$ (previously reported values are given for comparaison)[34]

			δ	$\Delta E_Q/2\varepsilon$	B_{hf}	τ
$Fe_2F_5(H_2O)_2$						
300 K	2 doublets	Fe^{3+}	0.48	0.58	-	0.52
		Fe^{2+}	1.31	2.50	-	0.48
77 K	2 doublets	Fe^{3+}	0.55	0.58	-	0.50
		Fe^{2+}	1.46	3.27	-	0.50
$Fe_3F_8(H_2O)_2$						
300 K	2 doublets	Fe^{3+}	0.46 (0.47)	0.54 (0.54)	-	0.66
		Fe^{2+}	1.34 (1.40)	2.13 (2.22)	-	0.34
77 K	1 sextuplet	Fe^{3+}	0.58 (0.57)	0.20 (0.20)	51.4 (51.3)	0.67
	1 doublet	Fe^{2+}	1.45 (1.47)	3.36 (3.39)	-	0.33

δ, ΔE_Q and 2ε are given in $mm.s^{-1}$, B_{hf} in T

3.2 Thermal behavior and stabilization of iron hydroxyfluorides

$Fe_2F_5(H_2O)_2$ and stabilisation of pyrochlore. The thermal behaviour of $Fe_2F_5(H_2O)_2$ was first investigated under inert atmosphere (N_2) by combined thermogravimetry (TGA) and mass spectrometry experiments. The TGA trace together with the ionic curves corresponding to the mass fragments m/z = 17 (OH^+), 18 (H_2O^+), 19 (F^+) are reported in **Figure 4a**. The absence of +19 signal indicates that the measured weight loss is only associated with the dehydration of $Fe_2F_5(H_2O)_2$. Moreover, the corresponding weight loss related to the dehydration process indicates a loss of 2 water molecules per formula unit as shown in reaction 1 and in agreement with a previous study.[40]

$$Fe_2F_5(H_2O)_2 \rightarrow FeF_3 + FeF_2 + 2H_2O \qquad (1)$$

The thermal behavior of $Fe_2F_5(H_2O)$ was further investigated under ambient humid air and dry air **(Figure 4b**) showing noticeable differences as compared to N_2. The first weight loss between 180°C and 240°C is lower than that corresponding to the dehydration process. This implies the concomitant loss of water molecules and oxidation of Fe^{2+} to Fe^{3+}. We experimented that this process is independent of the type of air we have used. Based on the experimental weight loss (11.3wt% under ambient air, 11.4wt% under dry air), we hypothesized the stabilization of anionic-deficient compound corresponding to $Fe^{3+}F_{2.5}O_{0.25}\square_{0.25}$ (calc: 11.5wt%) according to reaction (2) :

$$Fe^{2+}Fe^{3+}F_5(H_2O)_2 + ¼\ O_2 \rightarrow 2\ Fe^{3+}F_{2.5}O_{0.25}\square_{0.25} + 2H_2O \qquad (2)$$

Above 500°C, the lacunar oxyfluoride is hydrolysed into Fe_2O_3 according to reaction (3) (exp: 22.1% under ambient air, exp: 21.9% under dry air, calc: 22.6%):

$$2\ Fe^{3+}F_{2.5}O_{0.25}\square_{0.25} + 5/2\ H_2O \rightarrow Fe_2O_3 + 5HF \qquad (3)$$

To follow the structural changes induced by the thermal treatment of $Fe_2F_5(H_2O)_2$, X-ray thermodiffraction was performed under dry air. It reveals that $Fe_2F_5(H_2O)_2$ is stable up to 200 °C and then decomposes into a crystalline phase between 200 °C and 300 °C with a structure close to that of pyrochlore FeF_3 **(Figure 4c)**. Above 300 °C, this intermediate phase transforms slowly into hematite α-Fe_2O_3 in agreement with TGA measurement.

Figure 4. Thermogravimetric curves under N_2 atmosphere (a), ambient air or dry air (b) and thermal evolution of the X-ray diffractograms under dry air of $Fe_2F_5(H_2O)_2$ (c).

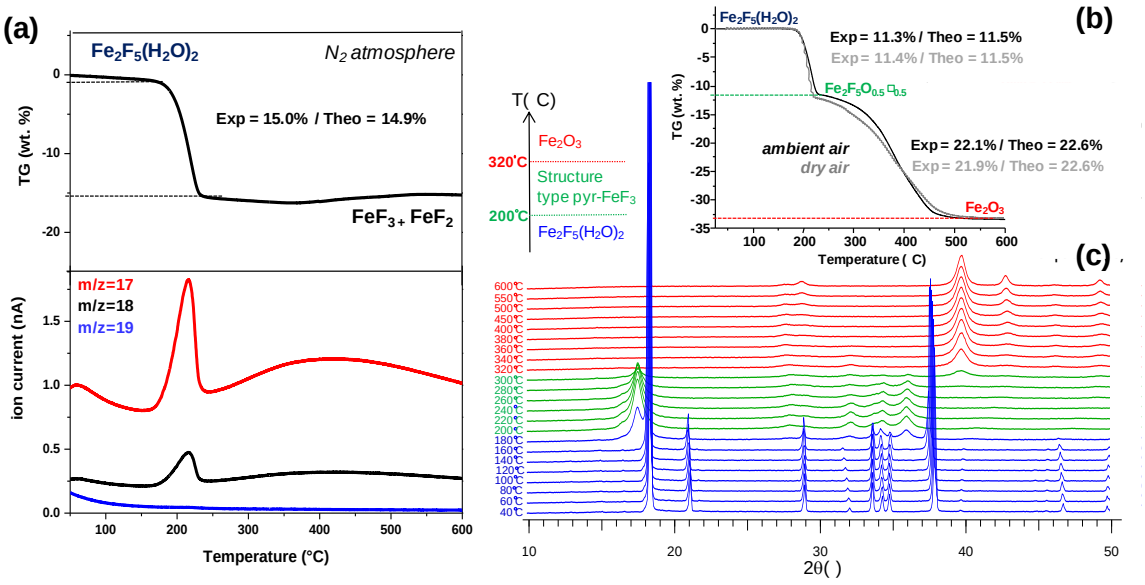

To investigate the formation of an anion-deficient oxyfluorinated phase, $Fe_2F_5(H_2O)_2$ was decomposed under air at 200 °C (1 h). The atomic structure of the prepared sample was probed by the pair distribution function (PDF) method obtained by Fourier transformation of the

correlation function.[41] PDF describes structural features across different scales, giving information on inter-atomic distances (*r*) at short-, intermediate- and long-range order.[42] It has been previously demonstrated that the stabilization of anionic vacancies induces local structural rearrangements which can be observed at small interatomic distances, *i.e.*, $r < 10$ Å.[43] Hence, we attempted to refine the PDF data against a structural model based on the pyrochlore structure. The PDF refinement (**Figure 5**) agrees well with the experimental data. Noticeably, at $r < 10$ Å, the structural model allows the PDF features to be reproduced, thus indicating the absence of any local distortion that would be induced by the presence of anionic vacancies.

Figure 5. PDF refinement of $Fe_2F_5(H_2O)_2$ decomposed at 200 °C (1h).

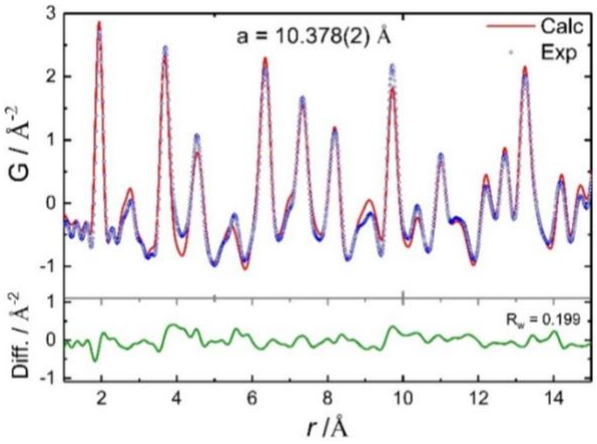

The presence of anionic vacancies can be also *a priori* excluded according to Mössbauer results. Indeed, the Mössbauer quadrupolar spectra obtained at 300 K and 77 K illustrated in **Figure 6** indicate unambiguously the exclusive presence of high spin Fe^{3+} species confirming the oxidation of Fe^{2+} during the decomposition. To account for the ferric quadrupolar doublet with asymmetrical profile, different fitting models involving a discrete number of independent quadrupolar components were assumed at both 300 K and 77 K, but their fine interpretation remains unclear. The best compromise is finally obtained when a discrete distribution of

quadrupolar splitting linearly correlated to that of isomer shift is considered: the range of isomer shift δ values is consistent with Fe^{3+} species surrounded by F^- and OH^-/O^{2-} ions while the mean δ values (<0.415(10)> and <0.545(10)> at 300 and 77 K, respectively) suggest an excess of F^- compared to OH^-/O^{2-} ions.

Figure 6. ^{57}Fe Mössbauer spectra at 300 K and 77 K of $Fe_2F_5(H_2O)_2$ decomposed at 200 °C (1h).

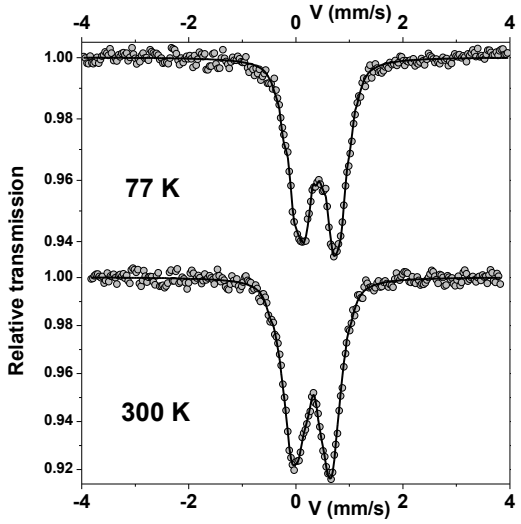

In order to study the stability of the anion-deficient iron oxyfluoride, $Fe^{3+}F_{2.5}O_{0.25}\square_{0.25}$, a TGA experiment under ambient air was realized up to the end of the first weight loss and the sample was immediately cooled (10 °C/min) at 30 °C (**Figure 7a**). On cooling at room temperature, $Fe^{3+}F_{2.5}O_{0.25}\square_{0.25}$ reacts rapidly with water molecules. Iron cations with anionic vacancies act as Lewis acids giving very attractive sites for H_2O species and leading to the formation of a phase that can be written $Fe^{3+}F_{2.5}O_{0.25}(H_2O)_{0.25}$ or $Fe^{3+}F_{2.5}(OH)_{0.5}$. A TGA analysis of this compound under ambient air until 600 °C confirms the formulation: the total weight loss is 28.5% (calc: 29.1%) (**Figure S1**). The loss and gain of water molecules under ambient air as a function of the treatment temperature were also followed by infrared spectroscopy performed at room temperature (**Figure 7b**). The FTIR spectrum of $Fe_2F_5(H_2O)_2$ presents two bands between 3000 and 3500 cm^{-1} and at 1625 cm^{-1} that are attributed respectively to the stretching and bending

modes of structural water molecules. On heating at increasing temperatures and further cooling in ambient conditions, these absorption bands decrease and other new intense peaks at 1090 and 1170 cm^{-1}, attributed to OH groups, appear.[44] This feature is consistent with the formation of the iron hydroxyfluoride $Fe^{3+}F_{2.5}(OH)_{0.5}$. The weight loss after treatment in the oven at 200 °C for 1 h is 7.5%. The instability of $Fe^{3+}F_{2.5}O_{0.25}\square_{0.25}$ under air at room temperature is clearly evidenced; this lacunar oxyfluoride reacts with water to form a stable hydroxyfluoride according to reaction 4:

$$Fe^{3+}F_{2.5}O_{0.25}\square_{0.25} + 1/4\ H_2O \rightarrow Fe^{3+}F_{2.5}(OH)_{0.5} \qquad (4)$$

Figure 7. TGA under ambient air of $Fe_2F_5(H_2O)_2$ up to the end of the first weight loss and cooling at RT (a), evolution of the IR spectra of $Fe_2F_5(H_2O)_2$ after treatment under air atmosphere at increasing temperatures (b).

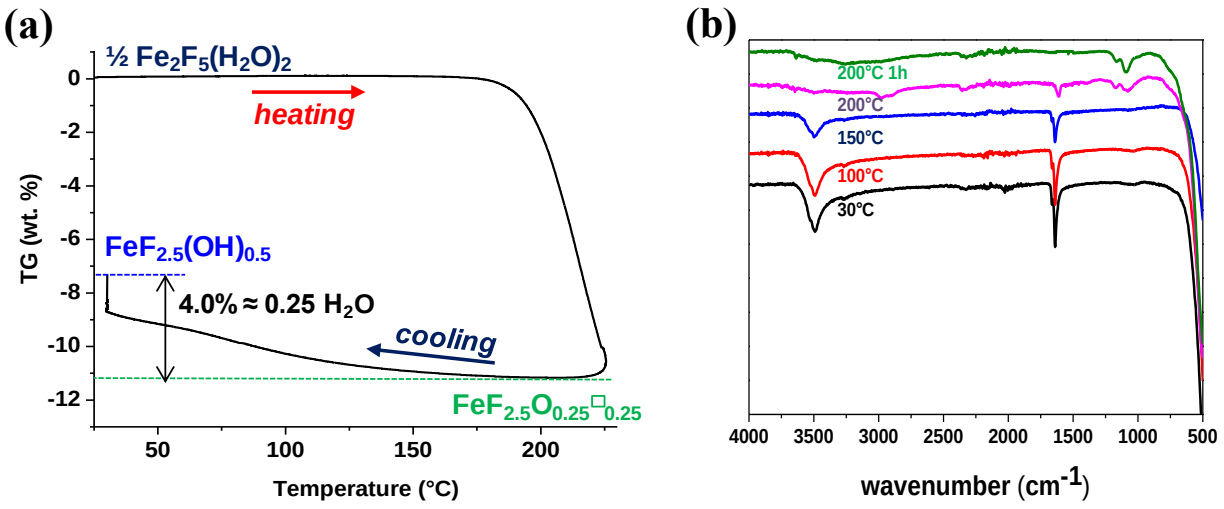

A Rietveld analysis of the X-ray powder diffraction data was further conducted on $FeF_{2.5}(OH)_{0.5}$. R. De Pape *et al.* first identified and determined the crystal structure of pyrochlore type FeF_3 (ICSD-202047, FeF_3, cubic, *Fd*-3*m* space group, a = 10.325 Å, V = 1100.7 $Å^3$). In $FeF_{2.5}(OH)_{0.5}$, the presence of OH groups is evidenced so that we considered a structural model based on iron

atoms located in 16c sites and on 48f sites statistically occupied by fluorine atoms (83.3%) and oxygen atoms (16.7%). The refinement of $FeF_{2.5}(OH)_{0.5}$ with the pyrochlore structure and with empty tunnels gives an unsatisfying fit of experimental data ($R_F = 0.121$, $R_B = 0.074$) (Table S4). Despite the storage of the sample in a glovebox, the presence of water molecules (Ow), inserted during the sample preparation for X-ray diffraction and located in the interconnecting open channels, cannot be excluded. Consequently, water molecules are introduced in 8b sites (3/8, 3/8, 3/8) affording good reliability factors (R_B = 0.067, R_F = 0.048,) and leading to $FeF_{2.5}(OH)_{0.5}\cdot 0.5H_2O$ formulation **(Figure 8a,b)**. The Fe-O/F distances, equal to 1.924(2) Å, are very close to that found in pyrochlore FeF_3 (1.929 Å).

Figure 8. Final Rietveld fit of the X-ray powder diffraction pattern with a representation of pyrochlore $FeF_{2.5}(OH)_{0.5}\cdot 0.5H_2O$ (structure in insert) (a) and structural parameters (b).

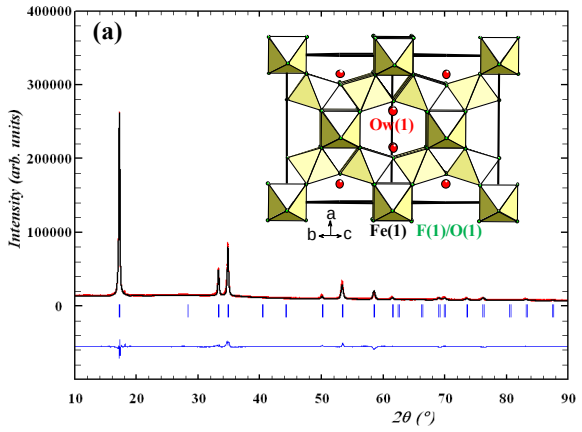

(b)

Cubic *Fd*-3*m*, a = 10.3571(4) Å, V = 1111.0(1) Å^3

R_B = 0.064, R_F = 0.048

Atom	Wyck.	τ (%)	x	y	z	B(Å^2)
Fe(1)	16c	100	0	0	0	1.0(1)
F(1)	48f	83.3	0.3067(3)	1/8	1/8	1.7(2)
O(1)	48f	16.7	0.3067(3)	1/8	1/8	1.7(2)
Ow(1)	8b	100	3/8	3/8	3/8	7.2(5)

Fe(1)-F(1)/O(1) = 1.924(2) Å

ΣFe(1) = +3.17

$Fe_3F_8(H_2O)_2$ and stabilisation of HTB structure. A similar methodology is applied to study the thermal behaviour of $Fe_3F_8(H_2O)_2$. Under N_2 atmosphere, the dehydration of $Fe_3F_8(H_2O)_2$ leads to a phase mixture of FeF_3 and FeF_2 **(Figure S2)** without iron oxidation :

$$Fe_3F_8(H_2O)_2 \rightarrow 2FeF_3 + FeF_2 + 2H_2O \qquad (5)$$

Under air atmosphere, the thermal behaviour of $Fe_3F_8(H_2O)_2$ is significantly influenced by the presence of water. **Figure 9a** gathers the TGA curves measured under ambient and dry air. It shows that $Fe_3F_8(H_2O)_2$ starts to decompose at 200 °C under ambient air and 220 °C under dry air: water molecules favour the decomposition of $Fe_3F_8(H_2O)_2$. After this first event, the final weight loss is similar in both dry and ambient air, suggesting the stabilization of compounds with close chemical compositions involving two concomitant reactions of dehydration and Fe^{2+} oxidation, and leading thus to an anion-defective composition $FeF_{2.66}O_{0.17}\square_{0.17}$. It should be noted that, unlike $Fe_2F_5(H_2O)_2$, the oxidation of Fe^{2+} in Fe^{3+} is not fully achieved; the defective oxyfluoride $FeF_{2.66}O_{0.17}\square_{0.17}$ is simultaneously formed with FeF_2 impurity phase (exp. weight loss: 9.7% for 14% FeF_2 under ambient air between 200°C and 300°C, exp: 9.6% for 13% FeF_2 under dry air between 220 °C and 320 °C).

After the formation of $FeF_{2.66}O_{0.17}\square_{0.17}$ and FeF_2, an ambient air atmosphere (not dry) leads to a complete hydrolysis of the mixture to form hematite Fe_2O_3 (exp: 22.0%, calc: 23.0%) while the mixture transforms very slowly into oxide under dry air.

X-ray thermodiffraction was further conducted under dry air to investigate the phase changes occurring during the thermal decomposition of $Fe_3F_8(H_2O)_2$ **(Figure 9b)**. It reveals that the structure is stable up to 260 °C. Above 260 °C, a crystalline intermediate with the HTB network, stable up to 360 °C, appears with a FeF_2 impurity (rutile structure). After hydrolysis above 360 °C, the final product is α-Fe_2O_3. The evolution of the IR spectra of $Fe_3F_8(H_2O)_2$ after treatment at increasing temperatures and cooling under air atmosphere shows the formation of an iron hydroxyfluoride $FeF_{2.66}(OH)_{0.34}$; the bands characteristic of water molecules decrease while the bands attributed to OH groups appear (**Figure 9c**). The best purity of $FeF_{2.66}(OH)_{0.34}$ is

obtained for a treatment at 300 °C for 1 h under ambient air; the molar percentage of FeF_2 is estimated to 5.0% by Mössbauer spectrometry, as discussed in the next section.

Figure 9. Thermogravimetric analyses under ambient air and dry air of $Fe_3F_8(H_2O)_2$ (a), thermal evolution of the X-ray diffractograms under dry air of $Fe_3F_5(H_2O)_2$ (b), evolution of the IR spectra of $Fe_3F_8(H_2O)_2$ after treatment under air atmosphere at increasing temperatures (c).

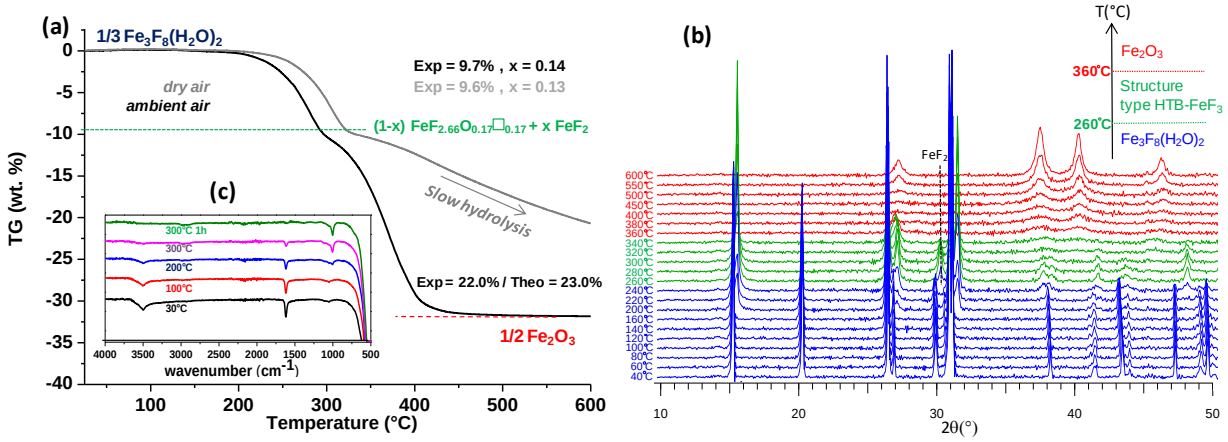

Similarly to $Fe_2F_5(H_2O)_2$, we cannot conclude on the stabilization of anion-deficient compound. Using PDF analysis, we indeed conclude on the absence local distortion that would have been induced by the presence of anionic vacancies (see SI). Mössbauer spectra of $FeF_{2.66}(OH)_{0.34}$ were recorded at 300 K and 77 K, as illustrated in **Figure 10**. At 300 K, a dominant central feature is clearly observed. It has to be described by means of at least two quadrupolar doublets attributed unambiguously to Fe^{3+} species: in addition, a small quadrupolar component assigned to ferrous species typical of FeF_2 allows a complete description of the baseline, particularly at about 2.2 mm/s. At 77 K, the magnetic splitting allows to distinguish 4 different magnetic components: 3 are clearly attributed to Fe^{3+} species while the last one is due to FeF_2 component. Consequently, the 300 K Mössbauer spectrum was also described by means of 4 components: it is important to emphasize that since the hyperfine structure appears to be rather

easily modeled, numerous fits can be considered at room temperature; the model reported in the present work is consistent with that obviously obtained from the 77 K spectrum. The refined values of hyperfine parameters are listed in **Table 2**. The values of the quadruplar splittings at 300 K can be compared to the literature values reported in Table S5, it can be concluded that the largest isomer shift values suggest F-rich environments of Fe^{3+} species and the smaller values to F and O environments.

Table 2. Refined values of hyperfine parameters of HTB-$FeF_{2.66}(OH)_{0.34}$.

			δ	$\Delta E_Q/2\varepsilon$	B_{hf}	τ
HTB-$FeF_{2.66}(OH)_{0.34}$						
300 K	4 doublets	Fe^{3+}	0.47	0.18	-	31
			0.46	0.57	-	36
			0.40	0.40	-	30
			<0.45>			
		Fe^{2+}			-	3
77 K	4 sextuplets	Fe^{3+}	0.57	0.08	53.1	29
			0.56	-0.05	51.0	37
			0.50	-0.04	43.4	27
			<0.55>			
		Fe^{2+}			-	5

δ, ΔE_Q and 2ε are given in $mm.s^{-1}$, B_{hf} in T

Figure 10. ^{57}Fe Mössbauer spectra at 300 K and 77 K of $FeF_{2.66}(OH)_{0.34}$.

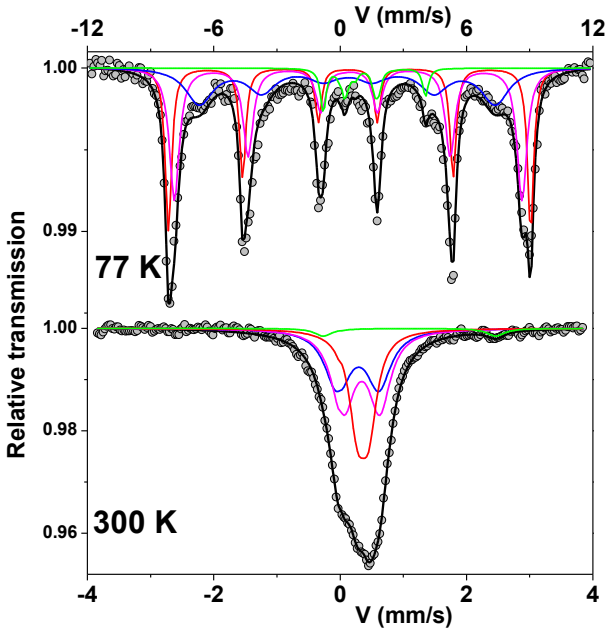

Powder XRD data recorded after thermal treatment and cooling show that $Fe_3F_8(H_2O)_2$ decomposes into a crystalline intermediate $FeF_{2.66}(OH)_{0.34}$ with HTB structure and 4.2 weight percent of FeF_2 (5.0% molar percent), as deduced from Mössbauer spectrometry. During Rietveld refinement, the FeF_2 content was constrained and only the overall isotropic displacement factor (B_{ov}) was refined, taking into account the low crystallinity of both fluorinated phases. For the HTB phase, a first solution based on the structural model of HTB-$FeF_3{\cdot}0.33H_2O$ was found (ICSD-35359, $FeF_3{\cdot}0.33H_2O$, orthorhombic system, *Cmcm* space group, a = 7.423 Å, b = 12.730 Å, c = 7.526 Å, V = 711.1 Å^3).[10] The assignment of O/F atoms in iron environments, deduced from the M-(O/F) distances was applied and a good fit of experimental data (R_B = 0.055, R_F = 0.072) was only obtained when water molecules were introduced in the hexagonal cavities and their site occupations are refined (Table S6): the $FeF_{2.66}(OH)_{0.34}{\cdot}0.13H_2O$ formulation resulted. In this *Cmcm* model, the 8f sites of F(1) atoms are statistically occupied by fluorine atoms (50%) and oxygen atoms (50%) (Table S7). However, the bond valence calculations are surprisingly different from the expected value for Fe^{3+} (Fe(1) =

+3.22 and Fe(2) = +2.68). The Fe(2)-F(1)/O(1) distance (2.18(1) Å) is very long while the intermolecular distance between fluoride atoms (F(1)/O(1)) and water molecule (Ow) in the cavities ($d_{F(1)/O(1)\cdots H\text{-}Ow(1)}$ = 2.13(3) Å) is too short (**Figure S3**). Consequently, a structural model of HTB-FeF_3 previously obtained from neutron data in the hexagonal $P6_3/m$ space group was considered.[45] The introduction of water molecules in the hexagonal cavities and a full occupation of 12i sites by fluorine atoms (83.3%) and oxygen atoms (16.7%), very satisfactory results (R_B = 0.068, R_F = 0.074), were obtained for the $FeF_{2.66}(OH)_{0.34}\cdot 0.21H_2O$ formulation (**Figure 11a**), in spite of better reliabilities in *Cmcm* space group. Iron cations lie at the center of distorted $Fe(1)F_6$ octahedra with two long Fe(1)-F(2)/O(2) distances (1.993(12) Å) and four short Fe(1)-F distances (1.901(8) Å and 1.929(2) Å). These distances lead to a good valence value of Fe^{3+} (Fe(1) = +3.04). Water molecules are distributed on partially occupied sites; they establish hydrogen bonds with F(2)/O(2) anions and the corresponding distances ($d_{F(2)/O(2)\cdots H\text{-}Ow(1)}$ = 2.51(2)-2.58(2) Å) which are acceptable (**Figure 11b,c**).

We further attempted to fit the experimental PDF of the HTB phase using either the *Cmcm* or the $P6_3/m$ space group. Although the values of goodness of fits are close, we noticed that, locally, the *Cmcm* based structure better agrees with the experimental data **(Figure S4)**. However, similarly to Rietveld analysis, bond valence calculations better agree with the $P6_3/m$ space group (Fe(1) = +3.02 and Fe(2) = +2.59 for *Cmcm* and Fe(1) = +2.99 for $P6_3/m$).

Figure 11. Final Rietveld fit of the powder X-ray pattern (a) with representation of the HTB structure $FeF_{2.66}(OH)_{0.34}\cdot 0.21H_2O$ (b) and structural parameters (c).

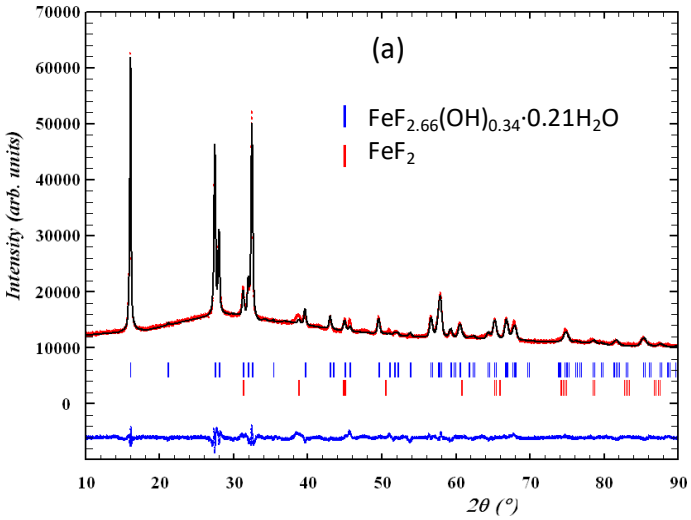

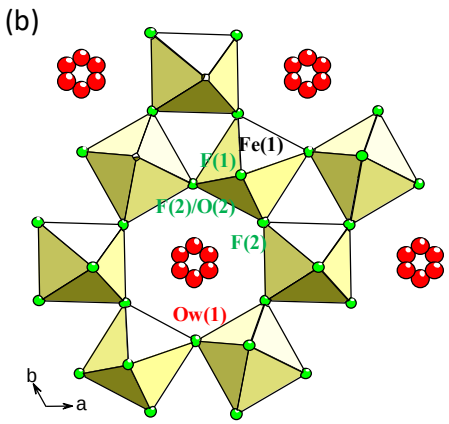

(c)

Atom	Wyck.	τ (%)	x	y	z
Fe(1)	6g	100	½	0	0
F(1)	6h	100	0.4617(9)	0.0241(11)	1/4
F(2)	12i	83.3	0.2136(14)	-0.2005(14)	0.0353(4)
O(2)	12i	16.7	0.2136(14)	-0.2005(14)	0.0353(4)
Ow(1)	12i	10.7	0.0425(19)	0.0851(19)	0.6469(16)

Hexagonal, $P6_3/m$
a = 7.396(1) Å, c = 7.545(1) Å
V = 714,7(1) $Å^3$
R_B = 0.068, R_F = 0.074, B_{ov} = 1.75(7) $Å^2$
2 x Fe(1)-F(1) = 1.901(8) Å
2 x Fe(1)-F(2) = 1.929(2) Å
2 x F(2)/O(2) = 1.993(12) Å
ΣFe(1) = +3.04

3.3 Electrochemical investigations

Electrochemical properties were investigated to examine the impact of the structural architecture, the loss of water molecules and the presence of hydroxyl groups on the Li reactivity mechanism. Four samples were tested: both pristine materials $Fe^{2+}Fe^{3+}F_5(H_2O)_2$ and $Fe^{2+}Fe^{3+}{}_2F_8(H_2O)_2$, and both hydroxyfluorides $Fe^{3+}F_{2.5}(OH)_{0.5}$ (pyrochlore) and $Fe^{3+}F_{2.66}(OH)_{0.34}$ (HTB). The cells were cycled between 2 and 4 V with a discharge cutoff voltage limited to 2 V vs Li^+/Li to avoid the conversion reaction that leads, below 2 V, to the formation of metallic Fe that coexist with Li_2O and LiF phases. Both fluoride hydrates exhibit a poor lithium insertion (< 0.1 Li^+) on the first discharge, most likely due the presence of structural water molecules within the hexagonal

channels that strongly hampers the lithium diffusion. The dehydrated phases in contrast show a greater electrochemical activity near ~3.2 V with a reversible capacity of 165 and 170 mAh.g^{-1} during the first discharge for the pyrochlore $Fe^{3+}F_{2.5}(OH)_{0.5}$ and HTB-$FeF_{2.66}(OH)_{0.34}$, respectively (**Figure 12a,b**). For both phases, out of the 0.6-0.7 Li^+ inserted on discharge solely 0.5 Li^+ can be removed on charge, hence leading to reversible and sustainable capacities of 100-110 mAh.g^{-1} upon cyling.

Figure 12. First cycle voltage-composition curves for Li/iron fluoride cells in LP30 electrolyte at a scan rate of 0.05C: (a) comparison of $Fe_2F_5(H_2O)_2$ and $FeF_{2.5}(OH)_{0.5}$ first cycles, (b) comparison of $Fe_3F_8(H_2O)_2$ and $FeF_{2.66}(OH)_{0.34}$ first cycles, (c) electrochemical cycling of $FeF_{2.5}(OH)_{0.5}$ (pyrochlore), (d) electrochemical cycling $FeF_{2.66}(OH)_{0.34}$ (HTB).

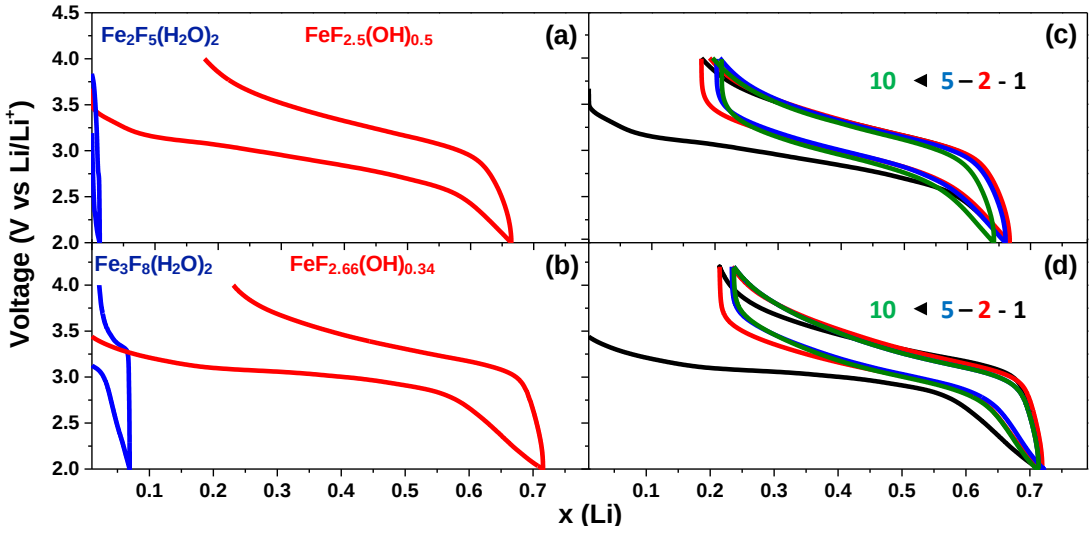

To explore the link between the redox process and the structural change, *in situ*-XRD was performed during the first discharge between 3.5 V (open circuit voltage: OCV) and 2 V (**Figure S5**). In the case of the pyrochlore $FeF_{2.5}(OH)_{0.5}$ sample, the 15°, 28°, 30°, and 50° peaks corresponding to the (111), (113), (222), and (044) reflexions persist after ball-milling with carbon SP, attesting the mechanical stability of the pyrochlore structure (**Figure 13a**). During the

electrochemical lithium insertion, a substantial amorphisation process is visible from $x_{Li+} > 0.5$ with a broadening of the Bragg peaks. This lithium insertion content coincides to the maximum of water in pyrochlore cavities of $FeF_3 \cdot 0.5H_2O$.[46-47]

For HTB-$FeF_{2.66}(OH)_{0.34}$, the structure persists also after ball-milling with carbon SP, showing distinctly the most intense HTB peaks (23.6° and 27.8°). However, upon intercalation of 0.35 Li, these peaks vanish and the HTB-structure disappears (**Figure 13b)**. In parallel, a new peak emerges at 23° and the crystallinity improves during lithium insertion. This feature suggests a strong structural similarity between the discharged phase and the ReO_3-type FeF_3 phase which exhibits an intense Bragg peak at 24°. Once again, the amount of Li^+ needed (0.35 Li^+) to trigger a phase change is equalled to the maximum amount of water inserted in the HTB-$FeF_3 \cdot 0.33H_2O$ structure.[12] This equality between the maximum amount of uptake Li^+ and H_2O in these compounds is not fortuitous. It is highly plausible that inserting more Li^+ ions or more H_2O inside the HTB structure triggers a structural rearrangement towards the ReO_3-type structure to the most thermodynamically stable of allotropic varieties of FeF_3, as previously observed by Dambournet *et al.*[31] The voltage profiles of the pyrochlore $FeF_{2.5}(OH)_{0.5}$ and HTB-$FeF_{2.66}(OH)_{0.34}$ phases after the first discharge are very similar; it can be supposed that the pyrochlore transforms into nanostructured FeF_3 with ReO_3-type during the lithium insertion.

Figure 13. *In situ* XRD during the first discharge between 3.5 V and 2 V of $FeF_{2.5}(OH)_{0.5}$ (pyrochlore) (a) and $FeF_{2.66}(OH)_{0.34}$ (HTB) (b).

(a) **(b)**

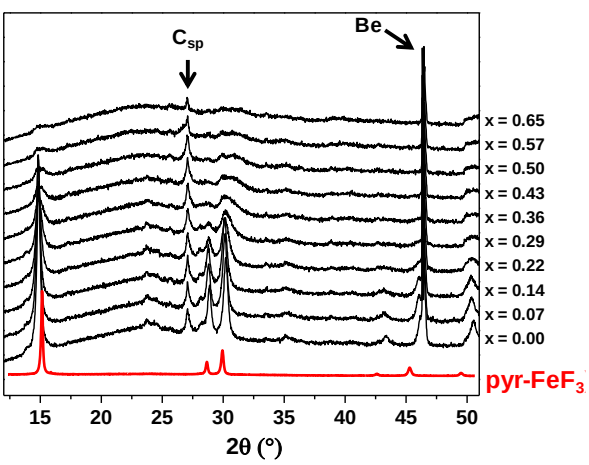
C_sp
Be
x = 0.65
x = 0.57
x = 0.50
x = 0.43
x = 0.36
x = 0.29
x = 0.22
x = 0.14
x = 0.07
x = 0.00
pyr-FeF3
15
20
25
30
35
40
45
50
2θ (°)

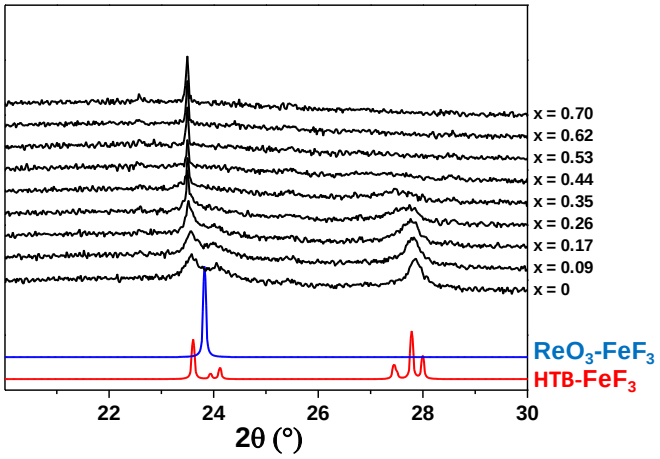
x = 0.70
x = 0.62
x = 0.53
x = 0.44
x = 0.35
x = 0.26
x = 0.17
x = 0.09
x = 0
ReO3-FeF3
HTB-FeF3
22
24
26
28
30
2θ (°)

CONCLUSION

From in depth-study of thermal behaviors of two known mixed valence Fe(II)/Fe(III) iron dehydrated fluorides, two metastable lacunar oxyfluorides transforming under ambient air into two stable iron hydroxyfluorides were evidenced. The two pristine samples $Fe^{2+}Fe^{3+}F_5(H_2O)_2$ and $Fe^{2+}Fe^{3+}{}_2F_8(H_2O)_2$ were solvothermally prepared under microwave heating and structurally characterized by powder X-ray diffraction and ^{57}Fe Mössbauer spectrometry. The thermal analyses (TGA, MS-TGA, HT-DRX) combined with Infra-Red spectroscopy and PDF analysis revealed that thermal behaviors are globally similar. Under nitrogen gas, a dehydration step following by a simple decomposition occurs. Under air, a concomitant dehydration step with an oxidation Fe^{2+}/Fe^{3+} leads to intermediate anion-deficient oxyfluorides $Fe^{3+}F_{3-2x}O_x\square_x$ (x = 0.25 and 0.17, respectively) and then, to a complete hydrolysis giving hematite α-Fe_2O_3 at higher temperatures. Both vacancies-containing oxyfluorides are instable under ambient atmosphere and transform rapidly into stable hydroxyfluorides formulated $Fe^{3+}F_{3-x}(OH)_x$ (x = 0.50 and 0.34, respectively) with open pyrochlore and HTB structures, respectively. The evaluation of the electrochemical properties in lithium cell shows that hydroxyfluorides could be good candidates as cathode materials with significantly sustained capacities even after several cycles. The *in situ*-XRD attest the stability both pyrochlore and HTB open structures and also suggest that the inserted lithium occupies the structural positions of water in the hexagonal channels of pyrochlore ($FeF_3 \cdot 0.5H_2O$) and HTB ($FeF_3 \cdot 0.33H_2O$) original structures. At the opposite, both pristine fluorinated hydrates exhibit very low lithium insertion as a consequence of closed channels by water molecules. As proved by Duttine *et al.*[30], it is expected that the presence of vacancies in intermediate anion-deficient oxyfluorides could increase the lithium insertion rates. Likewise, the partial substitution of iron cations by other transition metals such as Mn, Co or Ni

in dehydrated fluorides could have positive effects on electrochemical properties and could enable to identify a promising chemical composition as cathode material with a high capacity associated to a long-term cyclability.

ASSOCIATED CONTENT

Supporting Information

Crystal structure data and atomic coordinates of $Fe_2F_5(H_2O)_2$ and $Fe_3F_8(H_2O)_2$, TGA under ambient air of $FeF_{2.5}(OH)_{0.5}$, thermal analyses (thermogravimetry and mass spectrometry) of $Fe_3F_8(H_2O)_2$, crystallographic data of pyrochlore, ^{57}Fe Mössbauer Hyperfine Parameters of HTB and pyrochlore type phases known in the literature, crystallographic data of HTB type phases, representation of $FeF_{2.66}(OH)_{0.34}\cdot nH_2O$ in the two structural models, refinements of the PDF data of the HTB phase, voltage-composition profile of $FeF_{2.5}(OH)_{0.5}$ and $FeF_{2.66}(OH)_{0.34}$. This material is available free of charge via the Internet at http://pubs.acs.org.

AUTHOR INFORMATION

Corresponding Author

E-mail: jerome.lhoste@univ-lemans.fr (JL)

ORCID

Kévin Lemoine (KL): 0000-0003-0401-6416

Leiting Zhang (LZ): 0000-0003-4057-7106

Damien Dambournet (DD): 0000-0003-3831-2643

Jean-Marc Grenèche (J-MG): 0000-0001-7309-8633

Annie Ribaud (AR): 0000-0003-4845-5971

Marc Leblanc (ML): 0000-0001-7958-0359

Jean-Marie Tarascon (J-MT): 0000-0002-7059-6845

Vincent Maisonneuve (VM): 0000-0003-0570-953X

Jérôme Lhoste (JL): 0000-0002-4570-6459

ACKNOWLEDGMENTS

Thanks are due to the French Research Ministry for a doctoral grant (to KL).

The authors greatly acknowledge the responsible of platforms “Diffusion et Diffraction des Rayons X” and “Microscopy” of IMMM, Le Mans Université. The work done at the Advanced Photon Source, an Office of Science User Facility operated for the U.S. Department of Energy (DOE) Office of Science by Argonne National Laboratory, was supported by the U.S. DOE under Contract No. DE-AC02-06CH11357. K.L., D.D., V.M, and J.L. wish to thank the French fluorine network for continuous support.

REFERENCES

1. Armand, M.; Tarascon, J. M., Building better batteries. *Nature* **2008,** *451* (7179), 652-657.
2. Tarascon, J. M.; Armand, M., Issues and challenges facing rechargeable lithium batteries. *Nature* **2001,** *414* (6861), 359-367.
3. Kang, Y. K.; Kim, H. J.; Kim, E.; Oh, B.; Cho, J. H., Photocured PEO-based solid polymer electrolyte and its application to lithium-polymer batteries. *J. Power Sources* **2001,** *92* (1-2), 255-259.
4. C. P. Grey; J. M. Tarascon, Sustainability and in situ monitoring in battery development. *Nature Mater.* **2016,** 16 (1), 45-56.
5. Conte, D. E.; Pinna, N., A review on the application of iron(III) fluorides as positive electrodes for secondary cells. *Mater. Renew. Sustain. Energy* **2014,** *3* (4), 37.
6. Groult, H.; Tressaud, A., Use of inorganic fluorinated materials in lithium batteries and in energy conversion systems. *Chem. Commun.* **2018,** *54* (81), 11375-11382.
7. Amatucci, G. G.; Pereira, N., Fluoride based electrode materials for advanced energy storage devices. *J. Fluorine Chem.* **2007,** *128* (4), 243-262.
8. Cabana, J.; Monconduit, L.; Larcher, D.; Palacín, M. R., Beyond Intercalation-Based Li-Ion Batteries: The State of the Art and Challenges of Electrode Materials Reacting Through Conversion Reactions. *Adv. Mater.* **2010,** *22* (35), E170-E192.
9. Leblanc, M.; Pannetier, J.; Ferey, G.; De Pape, R., Single crystal refinement of the structure of rhombohedral FeF_3. *Rev. Chim. Mine.* **1985,** *22*, 107-114.
10. Leblanc, M.; Ferey, G.; Chevallier, P.; Calage, Y.; De Pape, R., Hexagonal tungsten bronze-type Fe^{III} Fluoride $(H_2O)_{0.33}FeF_3$ crystal-structure, magnetic properties, dehydration to a new form of iron trifluoride. *J. Solid State Chem.* **1983,** *47* (1), 53-58.
11. De Pape, R.; Ferey, G., A new form of FeF_3 with the pyrochlore structure : Soft chemistry synthesis, crystal structure, thermal transitions and structural correlations with the other forms of FeF_3. *Mater. Res. Bull.* **1986,** *21* (8), 971-978.
12. Calage, Y.; Leblanc, M.; Ferey, G.; Varret, F., Mössbauer investigation of hexagonal tungsten bronze type Fe^{III} fluorides: $(H_2O)_{0.33}FeF_3$ and anhydrous FeF_3. *J. Magn. Magn. Mater.* **1984,** *43* (2), 195-203.
13. Zu, C. X.; Li, H., Thermodynamic analysis on energy densities of batteries. *Energy & Environmental Science* **2011,** *4* (8), 2614-2624.
14. Badway, F.; Cosandey, F.; Pereira, N.; Amatucci, G. G., Carbon Metal Fluoride Nanocomposites: High-Capacity Reversible Metal Fluoride Conversion Materials as Rechargeable Positive Electrodes for Li Batteries. *J. Electrochem. Soc.* **2003,** *150* (10), A1318-A1327.
15. Chun, J.; Jo, C.; Sahgong, S.; Klin, M. G.; Lim, E.; Kim, D. H.; Hwang, J.; Kang, E.; Ryu, K. A.; Jung, Y. S.; Kim, Y.; Lee, J., Ammonium Fluoride Mediated Synthesis of Anhydrous Metal Fluoride-Mesoporous Carbon Nanocomposites for High-Performance Lithium Ion Battery Cathodes. *Acs Applied Materials & Interfaces* **2016,** *8* (51), 35180-35190.
16. Li, C.; Yin, C.; Gu, L.; Dinnebier, R. E.; Mu, X.; van Aken, P. A.; Maier, J., An $FeF_3 \cdot 0.5H_2O$ Polytype: A Microporous Framework Compound with Intersecting Tunnels for Li and Na Batteries. *J. Am. Chem. Soc.* **2013,** *135* (31), 11425-11428.

17. Zhao, E.; Borodin, O.; Gao, X.; Lei, D.; Xiao, Y.; Ren, X.; Fu, W.; Magasinski, A.; Turcheniuk, K.; Yushin, G., Lithium–Iron (III) Fluoride Battery with Double Surface Protection. *Adv. Energy Mater.* **2018,** *8* (26), 1800721.
18. Li, Y.; Zhou, X.; Bai, Y.; Chen, G.; Wang, Z.; Li, H.; Wu, F.; Wu, C., Building an Electronic Bridge via Ag Decoration To Enhance Kinetics of Iron Fluoride Cathode in Lithium-Ion Batteries. *ACS Applied Materials & Interfaces* **2017,** *9* (23), 19852-19860.
19. Zhang, R.; Wang, X.; Wei, S.; Wang, X.; Liu, M.; Hu, H., Iron fluoride microspheres by titanium dioxide surface modification as high capacity cathode of Li-ion batteries. *J. Alloys Compd.* **2017,** *719*, 331-340.
20. Ali, G.; Lee, J. H.; Chang, W.; Cho, B. W.; Jung, H. G.; Nam, K. W.; Chung, K. Y., Lithium intercalation mechanism into $FeF_3 \cdot 0.5H_2O$ as a highly stable composite cathode material. *Scientific Reports* **2017,** *7*, 8.
21. Bai, Y.; Zhou, X.; Zhan, C.; Ma, L.; Yuan, Y.; Wu, C.; Chen, M.; Chen, G.; Ni, Q.; Wu, F.; Shahbazian-Yassar, R.; Wu, T.; Lu, J.; Amine, K., 3D Hierarchical nano-flake/micro-flower iron fluoride with hydration water induced tunnels for secondary lithium battery cathodes. *Nano Energy* **2017,** *32*, 10-18.
22. Arico, A. S.; Bruce, P.; Scrosati, B.; Tarascon, J. M.; Van Schalkwijk, W., Nanostructured materials for advanced energy conversion and storage devices. *Nature Mater.* **2005,** *4* (5), 366-377.
23. Bruce, P. G.; Scrosati, B.; Tarascon, J. M., Nanomaterials for rechargeable lithium batteries. *Angewandte Chemie-International Edition* **2008,** *47* (16), 2930-2946.
24. Wei, S.; Wang, X.; Jiang, M.; Zhang, R.; Shen, Y.; Hu, H., The $FeF_3 \cdot 0.33H_2O$/C nanocomposite with open mesoporous structure as high-capacity cathode material for lithium/sodium ion batteries. *J. Alloys Compd.* **2016,** *689*, 945-951.
25. Yang, Z.; Zhang, Z.; Yuan, Y.; Huang, Y.; Wang, X.; Chen, X.; Wei, S., First-principles study of Ti doping in $FeF_3 \cdot 0.33H_2O$. *Current Applied Physics* **2016,** *16* (8), 905-913.
26. (a) Ali, G.; Rahman, G.; Chung, K. Y., Cobalt-doped pyrochlore-structured iron fluoride as a highly stable cathode material for lithium-ion batteries. *Electrochim. Acta* **2017,** *238*, 49-55; (b) Zhang, Z.; Yang, Z.; Li, Y.; Wang, X., Revealing the doping mechanism and effect of cobalt on the HTB-type iron fluoride: A first-principle study. *J. Phys. Chem. Solids* **2018,** *123*, 87-96.
27. Liu, M.; Wang, X. Y.; Wei, S. Y.; Hu, H.; Zhang, R.; Liu, L., Cr-doped $Fe_2F_5 \cdot H_2O$ with open framework structure as a high performance cathode material of sodium-ion batteries. *Electrochim. Acta* **2018,** *269*, 479-489.
28. Duttine, M.; Dambournet, D.; Penin, N.; Carlier, D.; Bourgeois, L.; Wattiaux, A.; Chapman, K. W.; Chupas, P. J.; Groult, H.; Durand, E.; Demourgues, A., Tailoring the Composition of a Mixed Anion Iron-Based Fluoride Compound: Evidence for Anionic Vacancy and Electrochemical Performance in Lithium Cells. *Chem. Mater.* **2014,** *26* (14), 4190-4199.
29. Burbano, M.; Duttine, M.; Borkiewicz, O.; Wattiaux, A.; Demourgues, A.; Salanne, M.; Groult, H.; Dambournet, D., Anionic Ordering and Thermal Properties of $FeF_3 \cdot 3H_2O$. *Inorg. Chem.* **2015,** *54* (19), 9619-9625.
30. Burbano, M.; Duttine, M.; Morgan, B. J.; Borkiewicz, O. J.; Chapman, K. W.; Wattiaux, A.; Demourgues, A.; Groult, H.; Salanne, M.; Dambournet, D., Impact of Anion Vacancies on the Local and Electronic Structures of Iron-Based Oxyfluoride Electrodes. *J. Phys. Chem. Lett.* **2019,** *10* (1), 107-112.

31. Dambournet, D.; Chapman, K. W.; Duttine, M.; Borkiewicz, O.; Chupas, P. J.; Groult, H., Lithium Insertion Mechanism in Iron-Based Oxyfluorides with Anionic Vacancies Probed by PDF Analysis. *ChemistryOpen* **2015**, *4*, 443.
32. Laligant, Y.; Pannetier, J.; Labbe, P.; Férey, G., A new refinement of the crystal structure of the inverse weberite $Fe_2F_5(H_2O)_2$. *J. Solid State Chem.* **1986,** *62* (2), 274-277.
33. Herdtweck, E., Die Kristallstruktur des gemischtvalenten Eisenfluoridhydrates $Fe_3F_8 \cdot 2H_2O$. *Z. Anorg. Allg. Chem.* **1983,** *501* (6), 131-136.
34. Leblanc, M.; Ferey, G.; Calage, Y.; De Pape, R., Idle spin behavior of the shifted hexagonal tungsten bronze type compounds $Fe^{II}Fe^{III}_2F_8(H_2O)_2$ and $MnFe_2F_8(H_2O)_2$. *J. Solid State Chem.* **1984,** *53* (3), 360-368.
35. Le Bail, A.; Duroy, H.; Fourquet, J. L., *Ab initio* structure determination of LiSbWO6 by X-ray powder diffraction. Mater. Res. Bull. **1988,** *23* (3), 447-452.
36. Rodríguez-Carvajal, J., Recent advances in magnetic structure determination by neutron powder diffraction. *Physica B: Condensed Matter* **1993,** *192* (1), 55-69.
37. Greneche, J. M.; Linares, J.; Varret, F.; Laligant, Y.; Ferey, G., Mössbauer spectroscopy of the magnetic behaviour of the frustrated series $AFeF_5(H_2O)_2$: A = Mn, Fe, Co, Ni. *J. Magn. Magn. Mater.* **1988,** *73* (1), 115-122.
38. Qiu, X.; Thompson, J. W.; Billinge, S. J. L. PDFgetX2: A GUI-Driven Program to Obtain the Pair Distribution Function from X-Ray Powder Diffraction Data. *J. Appl. Cryst.* **2004,** *37* (4), 678–678.
39. Farrow, C. L.; Juhas, P.; Liu, J. W.; Bryndin, D.; Božin, E. S.; Bloch, J.; Proffen, T.; Billinge, S. J. L. PDFfit2 and PDFgui: Computer Programs for Studying Nanostructure in Crystals. *J. Condens. Matter* **2007,** *19* (33), 335219.
40. Gallagher, K. J.; Ottaway, M. R., Mixed-valent iron fluoride hydrates and their thermal-decomposition products. *Dalton Trans.* **1975,** *11*, 978-982.
41. Keen, D. A. A Comparison of Various Commonly Used Correlation Functions for Describing Total Scattering. *J. Appl. Crystallogr*. **2001,** *34* (2), 172–177.
42. Billinge, S. J. L.; Kanatzidis, M. G. Beyond Crystallography: The Study of Disorder, Nanocrystallinity and Crystallographically Challenged Materials with Pair Distribution Functions. *Chem. Commun.* **2004,** *7*, 749–760.
43. Burbano, M.; Duttine, M.; Morgan, B. J.; Borkiewicz, O. J.; Chapman, K. W.; Wattiaux, A.; Demourgues, A.; Groult, H.; Salanne, M.; Dambournet, D., Impact of Anion Vacancies on the Local and Electronic Structures of Iron-Based Oxyfluoride Electrodes. *J Phys. Chem. Lett.* **2019,** *10* (1), 107-112.
44. Vimont, A.; Lavalley, J.-C.; Francke, L.; Demourgues, A.; Tressaud, A.; Daturi, M., Infrared Study of the Surface Properties of HTB-Type Al−, Cr−, Fe−Hydroxyfluorides. *J. Phys. Chem. B* **2004,** *108* (10), 3246-3255.
45. Leblanc, M.; De Pape, R.; Ferey, G.; Pannetier, J., Ordered magnetic frustration — V. Antiferromagnetic structure of the hexagonal bronzoid HTB-FeF_3; Comparison with the non frustrated rhombohedral form. *Solid State Commun.* **1986,** *58* (3), 171-176.
46. De Pape, R.; Ferey, G., Pannetier, J., A new form of FeF_3 with the pyrochlore structure : Soft chemistry synthesis, crystal structure, thermal transitions and structural correlations with the other forms of FeF_3. Mater. Res. Bull. 1986, 21 (8), 971-978.

47. Li, C.; Yin, C.; Gu, L.; Dinnebier, R. E.; Mu, X.; Van Aken, P. A.; Maier, J., An FeF_3•$0.5H_2O$ Polytype: A Microporous Framework Compound with Intersecting Tunnels for Li and Na Batteries. J. Am. Chem. Soc. **2013**, *135* (31), 11425-11428.

TOC GRAPHICS